# Novel Prototype of a Compton Camera Based on a Monolithic GAGG Crystal*

Lin Song,[1] Hao-Tian Qi,[1] and Li-Hua Zhu[1,†]

[1]*Beihang University, Beijing 100191, China*

Traditional scintillator-based or semiconductor-based Compton Cameras generally use the method of pixelation detector to obtain the interaction position of $\gamma$-rays with detectors, which suffers from the disadvantages of complex process, high cost, strong dependence on pixelation size for position resolution, and huge electronic readout system.These disadvanteages limit the development of miniaturization and commercialization of Compton Cameras. In this study, we used the whole GAGG crystal coupled Silicon Photomultiplier (SiPM) array to build two types of detectors, which are Side-readout type detector and Back- readout type detector, and developed two kinds of position reconstruction algorithm, the Response Function Method and the Photon Distribution Reconstruction Method. The position resolution of the two types of detectors was evaluated, and the position resolution of the Side-readout type detector and Back- readout type detector was 1.2 mm and 1.6 mm, respectively. In addition, we built a prototype of a double-layer Compton Camera based on a monolithic GAGG crystal using a Side-readout type detector as a scattering detector and a Back- readout type detector as an absorption detector. The position resolution of locating the radioactive source is 5.4 mm with the source placing 27 mm away from the scattering detector.

Keywords: Compton Camera, Scintillator, Position Reconstruction, SiPM

## I. INTRODUCTION

Compton Cameras use the principle of Compton scattering to locate where $\gamma$-rays are generated.It has unique advantage in detection efficiency compared with other gamma-ray imaging modalities since no mechanical collimation structure is needed.[1] Compton Cameras are widely used in the fields of biomedical and radiation environmental monitoring.[2–7]

In response to the enormous market demand, several foreign companies have carried out research and development of Compton Camera, and have successively released related products, such as United States H3D company released H100[8], PHDS company released GEGI[9], Japan Institute of Aerospace Sciences (ISAS) released ASTROCAM[10], etc. Among them, ASTROCAM has been tested on-site in Fukushima and has proven its capability for hot spot detection and radioactive decontamination assessment. The domestic Compton Camera imaging technology research is still in the development stage, and related simulation and image reconstruction algorithm research has been carried out one after another, such as: Guo Xiaofeng et al.[11] have carried out research on the Compton Camera composed of CZT detector based on Geant4. Some laboratories have built Compton Camera prototypes, such as Liu Yilin[12], Tsinghua University, built Compton Cameras based on 4×4 pixel 3-D CZT detectors; Zhang Jipeng et al.[13], Institute of High Energy Chinese Academy of Sciences, constructed a double-layer Compton Camera based on GAGG crystal and SiPM array. However, self-developed Compton Camera products that can be put on the market are still blank.

At present, whether it is scintillator-based or semiconductor-based Compton cameras, the interaction position of $\gamma$-rays is obtained by pixelating the detector[14–18]. Although the principle of this method is simple, it has obvious limitations that the reconstruction accuracy is completely dependent on the degree of pixelation of the detector. Scintillator crystals are prone to cracking and shattering during processing, making it difficult to obtain crystal arrays with small pixel sizes. Although semiconductor detectors can obtain small pixel sizes, semiconductor detectors themselves are expensive and difficult to promote. At the same time, both scintillator detection and semiconductor detection face a serious problem after increasing the degree of pixelation, that is, the unusually large electronic readout system. A bold and novel idea is to use a monolithic scintillator crystal for position reconstruction, which has the characteristics of simple structure, low cost, and easy storage compared with pixelated scintillator crystal arrays. There are very few reports of the use of monolithic scintillator crystals in Compton Cameras, mainly because it is difficult to confirm where $\gamma$-rays interact in the monolithic crystal. In recent years, with the increasing application of SiPM, this problem seems to be solvable. Traditional Compton Cameras use photomultiplier tubes (PMTs) as photoconversion devices, but PMTs are expensive, bulky and require high voltage, which cannot meet the needs of commercial Compton Cameras for low cost and miniaturization[19]. In contrast, SiPMs are small in size, high in gain, low in operating voltage, insensitive to magnetic fields, high in photon detection efficiency, and most importantly, they can be combined into any shape of detection arrays for use[20–23].

In this study, we constructed two types of detectors using the monolithic crystal coupled SiPM arrays to reconstruct the interaction position of $\gamma$-rays in the monolithic scintillator. The VMEDAQ system was used to obtain the relevant information of the interaction events in the detector. Two kinds of position reconstruction algorithm were developed to reconstruct the interaction positions of the events in the crystal, and the position resolution performance of the two types of detectors was evaluated experimentally. We used two types of

* Supported by the National Natural Science Foundation of China (No.U1867210)

† Corresponding author, Li-Hua Zhu, Beihang University, 13520056359, zhulh@buaa.edu.cn.

detectors as scattering detectors and absorption detectors for Compton Cameras, respectively, and developed a new prototype of Compton Camera, and experimentally tested the performance of this prototype.

## II. EQUIPMENTS

### A. The experimental equipment

Scintillators, such as NaI, CsI, Cerium-doped Gadolinium Aluminum Gallium Garnet(GAGG), LYSO, and $LaBr_3$, are often used in Compton cameras due to their relatively high detector efficiency and the fast time response.[24] The crystals used in this study were GAGG. Compared with other crystals, GAGG has the following advantages: 1. unlike NaI and $LaBr_3$, GAGG shows no non-hygroscopicity in air and does not need to be packaged; 2. Different from LYSO and $LaBr_3$, GAGG produces no internal background radiation; 3. GAGG has a higher luminescence yield and a shorter luminescence duration than the cases in CsI, which is conducive to improve the signal-to-noise ratio and energy resolution.[25, 26]

Traditional Compton Cameras use a pixelated crystal configuration, and the detector must be attached to the back of the crystal to match each pixel to get position information.[27] However, as a scattering detector, the Back-readout type detector will inevitably affect the outgoing $\gamma$-rays after interacting with the scattering detector, resulting in poor reconstruction results.In this study, a monolithic crystal was used, so a novel configuration the side-readout detector (referred to as S-type, figure 1.b) could be employed.At the same time, a Back-readout type detector (referred to as B-type, figure 1.c) was also built and used as an absorption detector for Compton Cameras. The S-type detector uses a 27*27*3 $mm^3$ GAGG crystal coupled with four 1*8 SiPM arrays(figure 1.a), and each SiPM is read out separately, with a total of 32 signals. The B-type detector uses a 27*27*2 $mm^3$ GAGG crystal coupled with an 8*8 SiPM array. The 8-channel SiPMs in horizontal of the 8*8 array are added into one signal output, so we get 8 outputs in horizontal. Similarly,the 8-channel SiPMs in longitudinal are added into one signal output, so we get 8 outputs in longitudinal. SensL's C-60035 pixel SiPM was selected, which has a pixel area of 3*3 $mm^2$. There are 10,998 micropixel APDs within each pixel, and each micropixel is 20 $\mu$m*20 $\mu$m in size. A double-layer Compton camera based on monolithic crystals was built, with an S-type detector as the scattering detector and a B-type detector as the absorption detector(figure 1.e). The distance between the scattering detector and the absorption detector is adjustable, and the distance used in this experiment is 20 mm. VMEDAQ is used to filter the coincidence events and log the amplitude of the signal.

### B. The S-type and B-type detector

The Cs-137 spectra measured by the S-type detector with and without the reflective layer are shown in figure 2(a,b), and the reflective layer material is polytetrafluoroethene. More fluorescent photons are collected when the reflective layer is wrapped, so the total energy peak address when the reflective layer is wrapped is significantly higher than that when the reflective layer is not wrapped. The resolution of the total energy peak is 8.2% when the reflective layer is wrapped, which is very close to the performance index value given by the crystal manufacturer. The energy resolution drops to 9.4% when don't wrap the reflective layer. The reflection layer has very little effect on the energy resolution of S-type detectors

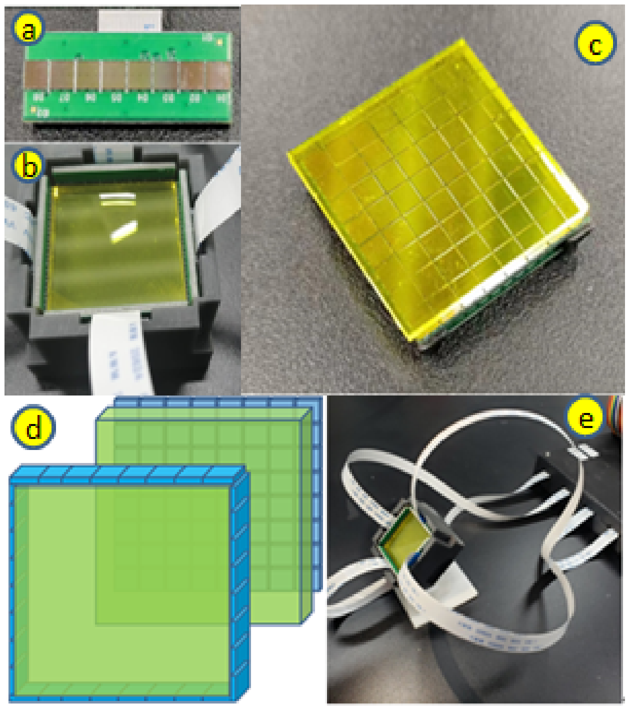


Fig. 1. a.1*8 SiPM array; b. S-type detector; c. B-type detector; d. the schematic diagram of the Compton camera; e. the prototype of the Compton camera

Due to the fact that the reflective layer is not completely smooth, the fluorescent photons are diffusely reflected by the reflector layer during transmission, so the interaction position information carried by them is destroyed. To study the impact of this destruction on S-type detector, we recorded the outputs of 32-channel SiPMs by irradiating the middle of the GAGG crystal vertically from a $\alpha$ source in two cases :with and without the reflective layer. As mentioned above, without reflective layer results in a slight reduction of the total energy peak address, so the amplification of the amplifier is slightly increased without the reflective layer. A similar operation is performed at B-type detector. For the S-type detector, 32-channel SiPMs are distributed on the four sides of the crystal. Due to the central symmetry, Figure 3(a,b) shows the spectrum of only 8-channel SiPMs on one side. The spectrum of SiPMs in the same geometric position on the left and right are very similar due to the left-right symmetry, so the spectrum of the 8-channel SiPMs can be divided into 4 groups. It can be seen that the spectrum difference between the four groups of SiPMs is not obvious when there is a reflective layer, which

will bring great uncertainty to reconstruct the interaction position. In the other hand if we don't wrap the reflective layer, the spectrum of the four groups of SiPMs has obvious differences, which is very beneficial for the determination of the interaction position.

For the S-type detector, the reflection layer only slightly improves energy resolution, but greatly reduces position resolution. In order to obtain better position resolution, the design of the S-type detector without the reflective layer was adopted.

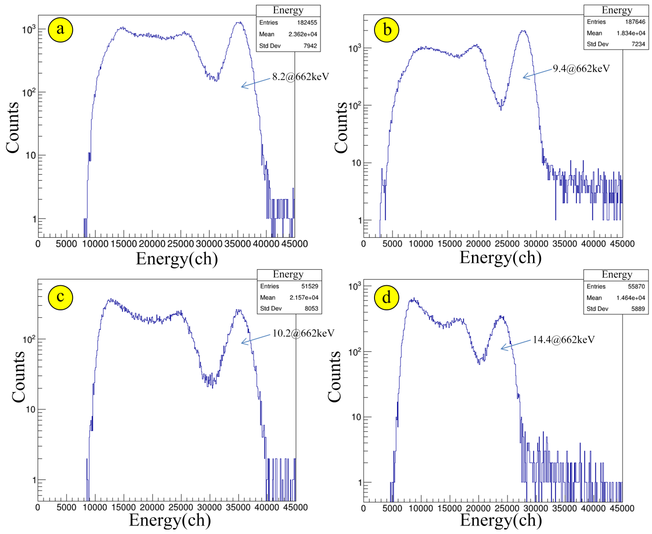


Fig. 2. The Cs-137 spectra of the S-type detector: with the reflective layer(a), without the reflective layer(b);The Cs-137 spectra of the B-type detector: with the reflective layer(c), without the reflective layer(d)

The Cs-137 spectra measured by the B-type detector with and without the reflective layer are shown in figure 2(c,d), and the reflective layer material is polytetrafluoroethene. Same as the S-type detector, for the B-type detector more fluorescent photons are collected, so the total energy peak address when the reflective layer is wrapped is higher,too. The energy resolution of the B-type detector is worse than that of the S-type detector no matter with or without the reflective layer. The main reason is that the B-type detector uses more SiPMs, and the impact of SiPM response inconsistent is greater. At the same time, the readout of the B-type detector in this study isn't one by one, but additive readout. The difference between additive circuits can also lead to a decrease in energy resolution.

The reflective layer reduces the energy resolution from 10.2% to 14.4% , which is a obvious reduction. It seems that the design of the B-type detector should be selected to wrap the reflective layer, but this study hopes to obtain better position resolution. The figure3(c,d) shows the spectrum of 8-channel outputs in the horizontal direction (the same in the vertical direction) with and without the reflective layer when the center of the B-type detector is irradiated with a $\alpha$ source. Due to the fixed irradiation position of the $\alpha$ source, theoretically, the energy spectrum of each output should be in the form of a Gaussian function. But in the case of wrapping the reflective layer, the energy spectrum of each channel deviates significantly from the Gaussian function. Because in this experiment, trig is set "or". If the reflective layer is not wrapped, it trig by fixed channel. But if wrapping the reflective layer, many channels may trig, resulting in the energy spectrum not the Gaussian function. Which may have a devastating impact on the position reconstruction, so the B-type still adopts the configuration without wrapping the reflective layer.

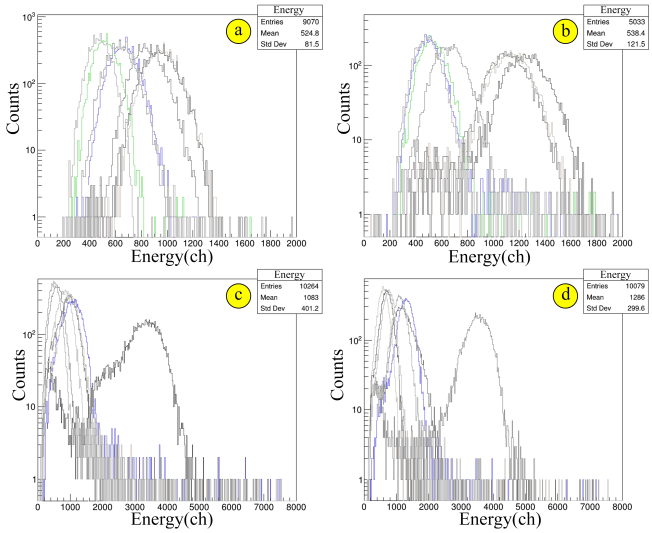


Fig. 3. the spectra of 8-channel SiPMs on the same side of the S-type detector when the interaction position is fixed at the center of the crystal: with the reflective layer(a), without the reflective layer(b); the spectra of 8-channel outputs of the B-type detector when the interaction position is fixed at the center of the crystal: with the reflective layer(c), without the reflective layer(d);

In order to improve energy resolution we will first measure the total energy of the scattering and absorbing detectors, pick out the events with the total energy as the full energy peak, and use the total energy minus the energy of the scattering detection to calculate the energy of the absorbing detector. In the future, the energy resolution can be improved by optimizing the B-type detector adduction circuit, or directly changing to the form of one by one readout.

### C. The interaction position scale experiment

Interaction position scale experiments in the detector were performed using the $\alpha$ source (Am-241, figure 4.b) and PCB masks(figure 4.a). The thickness of the PCB mask is 2 mm, and the hole diameter and the center spacing of adjacent holes remain unchanged in the same PCB mask. Multiple PCB masks with different hole diameters and hole spacing are used in this experiment, such as a PCB with a hole diameter of 1 mm and a hole distance of 3.4 mm (PCB ($\phi$1.0, D3.4)). The $\alpha$ source is placed in each hole in turn. The interaction position of these events is approximately considered to be the same position, and its coordinates x,y are taken from the co-

ordinates of the center of the hole,and its coordinates z is a fixed value (1.5 mm for the S-type detector and 1.0 mm for the B-type detector).(figure 4.c)

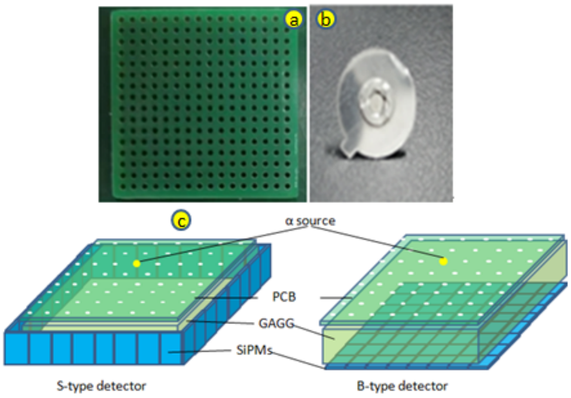


Fig. 4. The PCB mask(A),$\alpha$ source(B) The interaction position reconstruction experiment S-type and B-type detector(C)

## III. ALGORITHM

In this study, two kinds of reconstruction algorithm is developed to reconstruct the interaction position (x, y, z) where the $\gamma$-ray interacts with the detector: the response function method and the photon distribution reconstruction method. In both algorithm, z is taken as a fixed value. The response function method can be used to reconstruct the interaction position only for S-type detector, it's not work for B-type detector. The photon distribution reconstruction method can be used in both types of detector.

### A. The Response Function Method

Assuming that the scintillator is homogeneous and the fluorescence photons are emited uniformly in $4\pi$, so more fluorescent photons can be received, when the interaction point is closer to the SiPM. For example, the $\alpha$ sources are placed sequentially at 8 test points in the black box in figure 5(left). $E_{up}$ represents the energy deposited in the $SiPM_{up}$, and $E_{down}$ indicates the energy deposited in the $SiPM_{down}$. As the position of the interaction changes, the $E_{down}/E_{up}$ also changes, satisfying a certain response function, as shown in the figure 5(right). Repeating the above operations, the response functions of the whole detector (8 horizontal and 8 vertical) can be obtained. Then the x,y values of any event can be reconstructed by using these response functions. This algorithm is only applicable in S-type detectors because similar response functions cannot be obtained in B-type detectors.

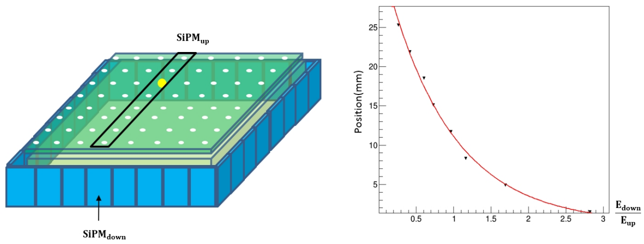


Fig. 5. 8 test points in a row(left), the response function(right)

### B. The Photon Distribution Reconstruction Method

When a single fluorescent photon is received by the SiPM, a pulse of a certain amplitude is produced as the output.When multiple fluorescent photons are received, the output signal is the superposition of all the fluorescent photon producing signals:

$$V_i = V_{i0} \cdot N_i \tag{1}$$

$V_i$ is the amplitude of the output signal of the $SiPM_i$, $N_i$ is the number of fluorescent photons received by the $SiPM_i$, $V_{i0}$ is the amplitude of the output signal when the $SiPM_i$ receives single fluorescent photon. The number of fluorescent photons received by the $SiPM_i$ is strongly correlated with the solid angle of the $SiPM_i$ subtended to the interaction position:

$$N_i = N_0 \cdot E \cdot \Omega_i \tag{2}$$

$N_0$ is the number of fluorescent photons per solid angle at the unit energy deposited, and E is the energy deposited at that point. Assuming that the fluorescence emission at the interaction position is uniform at $4\pi$, ignoring the fluorescence attenuation caused by the self-absorption of the crystal, then the $N_0$ is only a fixed value related to the luminescence yield of the crystal. $\Omega_i$ is the solid angle of the SiPM i subtended to the interaction position, as show in figure 6.

The ADC value of the SiPM i output signal is $ADC_i$:

$$ADC_i = a_i \cdot V_i + b_i \tag{3}$$

$a_i$ and $b_i$ are the scaling coefficients of the signal amplitude with the ADC address, which can be obtained experimentally and are fixed values.

$$\begin{aligned} ADC_i &= a_i \cdot V_{i0} \cdot N_0 \cdot E \cdot \Omega_i + b_i \\ &= K_i \cdot E \cdot \Omega_i + b_i \end{aligned} \tag{4}$$

When the unit energy is deposited in the crystal, the ADC value which the SiPM i receives photons in the unit solid angle can be calculated using the formula (4). $K_i$,$b_i$ are the conversion coefficient, can be measured experimentally. Before introduce the experiment, let's explain how to calculate $\Omega_i$.

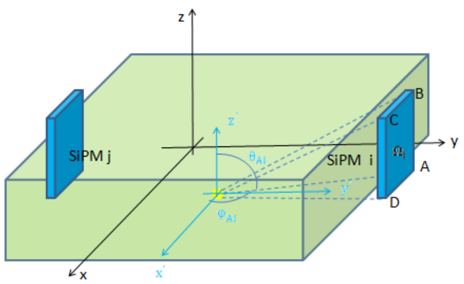


Fig. 6. The solid angle of the SiPM i and SiPM j subtended to the interaction position.

Taking the crystal center as the origin (0,0,0) of the xyz coordinate , the spatial coordinates of the 32 SiPMs have been determined, which is a known quantity. Taking $SiPM_i$ as an example, the coordinates of point A ($x_{Ai}$,$y_i$,$z_{Ai}$), point B ($x_{Bi}$,$y_i$,$z_{Bi}$), point C coordinates ($x_{Ci}$,$y_i$,$z_{Ci}$), and point D coordinates ($x_{Di}$,$y_i$,$z_{Di}$). $y_i$ is fixed values for the same SiPM . In this case, if an interaction occurs at any position in the crystal (x,y,z), the solid angle of $SiPM_i$ relative to the interaction position can be $\Omega_i$ obtained by integrating $\varphi_{Ai}$ and $\theta_{Ai}$ in the $x^{'}y^{'}z^{'}$ coordinate. In the $x^{'}y^{'}z^{'}$ coordinate system, the coordinates of the relative interaction positions of ABCD points are transformed into A($x_{Ai}$-x,$y_i$-y,$z_{Ai}$-z), point B coordinates ($x_{Bi}$-x,$y_i$-y,$z_{Bi}$-z), point C coordinates ($x_{Ci}$-x,$y_i$-y,$z_{Ci}$-z), and point D coordinates ($x_{Di}$-x,$y_i$-y,$z_{Di}$-z). There will be a slight change in $\theta$ during the integration from point A to point D, but this change is negligible unless the interaction position is very close to the SiPM. So in the following integration process, $\theta$ is considered unchanged from point A to point D.

$$\Omega_i = \int_{\varphi_{Ai}}^{\varphi_{Di}} \int_{\theta_{Ai}}^{\theta_{Bi}} sin\theta d\theta d\varphi \tag{5}$$

$$= \int_{\varphi_{Ai}}^{\varphi_{Di}} ((-cos\theta_{Bi}) - (-cos\theta_{Ai}))d\varphi \tag{6}$$

$$cos\theta_{Ai} = \frac{z_{Ai} - z}{\sqrt{((y_i - y)\cdot \frac{1}{tan\varphi_{Ai}})^2 + (y_i - y)^2 + (z_{Ai} - z)^2}} \tag{7}$$

suppose:

$$k_{Ai} = \frac{y_i - y}{z_{Ai} - z} \tag{8}$$

so:

$$cos\theta_{Ai} = \frac{1}{\sqrt{(\frac{k_{Ai}}{sin\varphi_{Ai}})^2 + 1}} \tag{9}$$

in the same way:

$$cos\theta_{Bi} = \frac{1}{\sqrt{(\frac{k_{Bi}}{sin\varphi_{Bi}})^2 + 1}} \tag{10}$$

Substituting the formula(5), formula(6) into the formula(3):

$$\Omega_i = \int_{\varphi_{Ai}}^{\varphi_{Di}} (\frac{1}{\sqrt{(\frac{k_{Ai}}{sin\varphi_{Ai}})^2 + 1}} - \frac{1}{\sqrt{(\frac{k_{Bi}}{sin\varphi_{Bi}})^2 + 1}})d\varphi \tag{11}$$

Here by looking up the indefinite integral table:

$$\int \frac{1}{(\frac{k}{sinx})^2 + 1} dx = \tag{12}$$

$$\frac{\sqrt{-1 - 2k^2 + cos^2x} \cdot cscx \cdot log(\sqrt{2}\cdot cosx + \sqrt{-1 - 2k^2 + cos2x})}{\sqrt{2 + 2k^2 \cdot csc^2x}} \tag{13}$$

$$k : constant \tag{14}$$

Equation (13) contains plural terms, but after merging and sorting, the plural terms are no longer existing, and the final result is:

$$\Omega_i = arctan(\frac{\sqrt{2k_{Ai}^2 + 2sin_{\varphi_{Ai}}^2}}{\sqrt{2}cos\varphi_{Ai}}) - arctan(\frac{\sqrt{2k_{Ai}^2 + 2sin_{\varphi_{Di}}^2}}{\sqrt{2}cos\varphi_{Di}})$$

$$+arctan(\frac{\sqrt{2k_{Bi}^2 + 2sin_{\varphi_{Ai}}^2}}{\sqrt{2}cos\varphi_{Ai}}) - arctan(\frac{\sqrt{2k_{Bi}^2 + 2sin_{\varphi_{Di}}^2}}{\sqrt{2}cos\varphi_{Di}}) \tag{15}$$

$$sin\varphi_{Ai} = \frac{y_i - y}{\sqrt{(y_i - y)^2 + (x_i - x)^2}} \tag{16}$$

$$cos\varphi_{Ai} = \frac{x_i - x}{\sqrt{(y_i - y)^2 + (x_i - x)^2}} \tag{17}$$

The transformations of $\varphi_{Bi}$ and $\varphi_{Di}$ are similar to those of $\varphi_{Ai}$.

The solid angle of the any interaction position to SiPMi can be calculated now. Next, the $K_i$,$b_i$ are measured experimentally.A $\alpha$ source was placed at any position in the crystal, the solid angle of the 32-channel SiPMs were theoretically calculated, and the ADC value of the 32-channel SiPMs were recorded experimentally. Then, the position of the $\alpha$ source was changed, the solid angle of the 32-channel SiPMs were calculated theoretically, and the ADC value of the 32-channel SiPMs were recorded experimentally. Theoretically, the values of $K_i$,$b_i$ can be obtained in two experiments, and in order to reduce the experimental error, the method of multiple experimental iterations of $K_i$,$b_i$ is adopted. The decision condition for the iteration is that the difference between the center value of the 32-channel SiPMs experimental energy spectrum

(the blue line in figure 7) and the theoretical calculated expected value (the red line in figure 7) is the smallest. The figure 7 shows the comparison of the 32-channel experimental energy spectrum and the theoretical calculated expected value at a certain experimental point. The $K_i$,$b_i$ ensure that the total difference between the theoretical and experimental values of the 32 SiPMs is smaller, so the experimental center value is slightly different from the theoretical calculated value in some SiPMs.

The Photon Distribution Reconstruction Method is not directly using the ADC value to calculate the position.The values of the 32-channel ADC at the interaction position can be calculated using Equation (4). First,32-channel ADC values are counted as a set of data at one interaction position. Then change the interaction position to get another set of data. Finally, repeat the process to make a database. When an unknown interaction position event occurs, a set of 32-channel ADC values is obtained, and the 32 ADC values are compared with each set of data in the database to find the most similar set of interaction position. The set that can best reproduce the photon distribution of the signal is the reconstructed position. Therefore, the larger the database, the higher the accuracy of the reconstruction. Experimentally, it's hard to make a large database. But using Equation (4), we can make a database of any size.

The solid angle of the SiPMi relative to any interaction position in the figure 6 can be calculated using the formula (15), which is only a schematic diagram of the S-type detector. If the crystal in the figure 6 is compressed in the y direction and elongated in the z direction, the schematic diagram of the B-type detector is obtained, so the formula (15) is still valid for the B-type detector.Therefore, the photon distribution reconstruction method can also be applied to B-type detectors.

## IV. RESULT

### A. The reconstruction result of the Response function method

Figure 8 shows the experimental results of the reconstruction using PCB ($\phi$1.0, D3.4) using the response function method. The red dot is the hole position of PCB ($\phi$1.0, D3.4) in the experiment, and the black dot is the central value of the reconstruction position, and the uncertainty is the FWHM (full width at half maximum) of the reconstruction position of the same hole event. Approximately 3,000 reconstruction events were counted at each experimental site.

As can be seen from the figure, the central value of the reconstruction position is basically the same as the experimental position, the average deviation of the 64 experimental points is about 0.3 mm(both the x and y direction). There is obvious deviation in data of the second to last, around 5 mm in vertical axis, comparing with other results. The reason is that the response function in figure 5 (right) changes rapidly around 5 mm. Due to the lack of experimental points, the response function cannot well describe the trend change of this part, resulting in poor position reconstruction results in this part. The uncertainty of the reconstruction position is relatively large. The main reason for these problems is that only part of the fluorescent photons are collected by each SiPM, and the statistical fluctuation of the fluorescence photon number is very large, so it is necessary to use as many SiPMs as possible to reduce the impact of statistical fluctuations when reconstructing the location.

### B. The reconstruction result of the Photon Distribution Reconstruction Method.

The reconstruction results of the photon distribution reproduction method are shown in figure 9 (S-type detector, PCB ($\phi$1.0, D3.4),left)and figure 9 (B-type detector, PCB ($\phi$1.0, D3.4),right). The red dot is the hole position of PCB ($\phi$1.0, D3.4) in the experiment, and the black dot is the central value of the reconstruction position, and the uncertainty is the FWHM (full width at half maximum) of the reconstruction position of the same hole event. Approximately 3,000 reconstruction events were counted at each experimental site.

The whole crystal is divided into two parts: the middle 6*6 36 experimental points and the outermost circle of 28 experimental points, the middle 6*6 is called the central part, and the outermost circle is called the edge part. For the S-type detector, the average deviation of the experimental points is about 0.3 mm(both the x and y direction) in the central part, which is same as the response function method. For the B-type detector, the average deviation of the experimental points is about 0.4 mm(both the x and y direction) in the central part, which is slightly higher than the response function method. In the edge part, the average deviation become 0.5 mm(both the x and y direction) for the S-type detector ,and 0.7 mm for the B-type detector. Because the closer to the edge of the crystal, the more serious the damage to the position information caused by the optical scattering of fluorescence.

The above reconstruction results show that the event with the interaction location at the edge part of the detector is not as good as the event in the center part. In the next experiment to determine the position-resolved limit, the edge part of the event will not be considered, and the event in the center of the detector will be mainly focused.

### C. The position-resolved limit experiments

The position resolution limit has been investigated by applying PCB masks with the different hole spacing. In order to reduce the uncertainty of the interaction position caused by the hole size, the hole diameter of the PCB board with a hole spacing of less than 2 mm is changed to 0.5 mm. Figure 10(up) shows the position reconstruction result (x-direction projection) using the PCB($\phi$0.5,D1.2) for the S-type detector, and Figure 10(down) shows the position reconstruction result (x-direction projection) using the PCB($\phi$0.5,D1.6) for the B-type detector.

The reconstruction algorithm used in the position-resolved limit experiment is the photon distribution reproduction method, which is used for both S-type and B-type detectors.

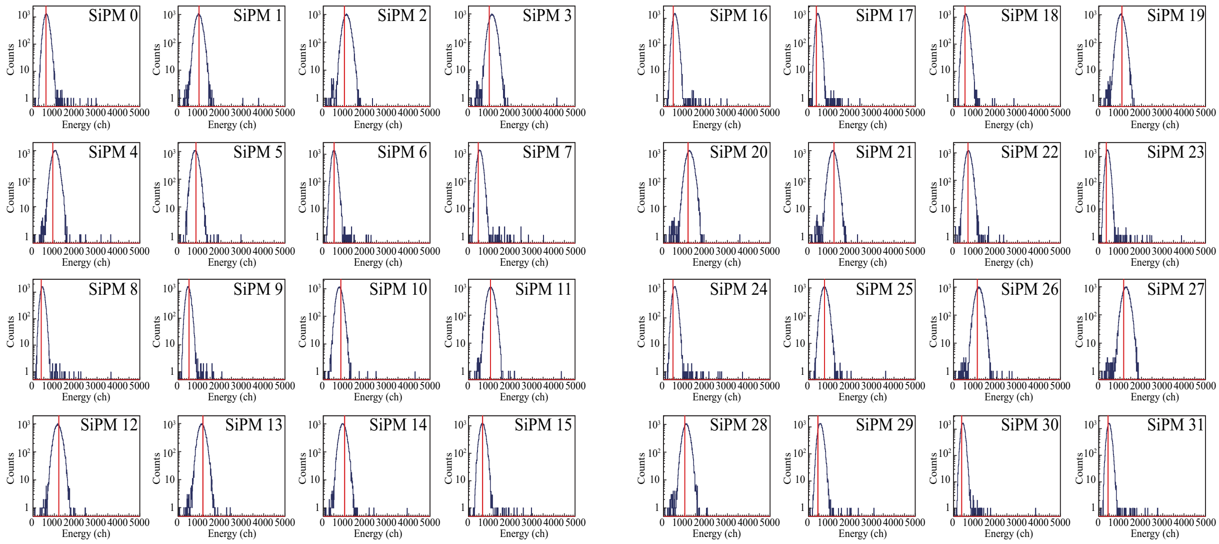


Fig. 7. the 32-channel experimental energy spectrum(blue line) and the theoretical calculated expected value(red line) at a certain experimental point

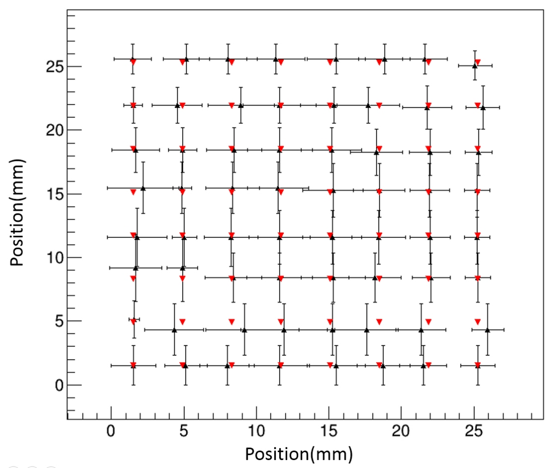


Fig. 8. The reconstruction result of the response function method(S-type detector, PCB (1.0, 3.4))

The figure 10(up) shows a total of 11 peaks from 8 mm to 22 mm, and the average spacing between the two peaks is about 1.27 mm, which is basically the same as the 1.2 mm hole spacing of the PCB board, indicating that the position resolution limit of the S-type detector is about 1.2 mm.

The figure 10(down) shows a total of 12 peaks from 5.5 mm to 26 mm,and the average spacing between the two peaks is about 1.71 mm, which is slightly larger than the 1.6 mm hole spacing on the PCB board, indicating that the position resolution limit of the B-type detector is about 1.6 mm. The reason why the position resolution limit is 1.6 mm instead of the more conservative 1.7 mm is that except for peaks 2,3 and peaks 9,10, which overlap significantly, the other peaks are very well distinguished, which should further reduce the hole spacing of the PCB. The reason for the overlap of peaks 2,3 and peaks 9,10 is that the positions of the holes of peaks 3 and 9 are exactly the gap positions of the two SiPMs in the SiPM array, and the gap width of the two SiPMs is about 0.43 mm, which is basically the same as the hole diameter of the PCB board of 0.5 mm. When the interaction sites are located at peaks 3 and 9, a large number of fluorescent photons are not received by the SiPMs, but escape through the gap between the SiPMs, which also explains why the counts at peaks 3 and 9 are significantly smaller. This problem does not exist for the S-type detector, where the S-type detector uses 32 SiPMs for position reconstruction at the same time, and when the interaction position is in the gap between one of the two SiPMs, the remaining 30 SiPMs can be used for position reconstruction without particularly affecting the reconstruction results.

## V. THE COMPTON CAMERA PRINCIPLE PROTOTYPE AND PERFORMANCE TESTING

A double-layer Compton Camera based on monolithic crystals was built, with an S-type detector as the scattering detector and a B-type detector as the absorption detector(figure 1.e). The spacing between the scattering detector and the absorption detector was 20 mm. Cs-137 point source (about 1 mm in diameter) was used as the imaging object in this study. The Cs-137 was placed two positions 27 mm away from the vertical direction of the scattering detector, and the two positions were 8 mm apart in the same imaging plane. Both the S-type detector and the B-type detector use the Photon Distribution Reconstruction Method to reconstruct the interaction position. Figure 11 shows the reconstruction results for the two positions. Use the FWHM of the reconstruction result as the spatial resolution, so the spatial resolution at 27 mm is about 5.4 mm.

Compared with the existing Compton Cameras, Turecek et al.[28] developed a double-layer Compton Camera composed

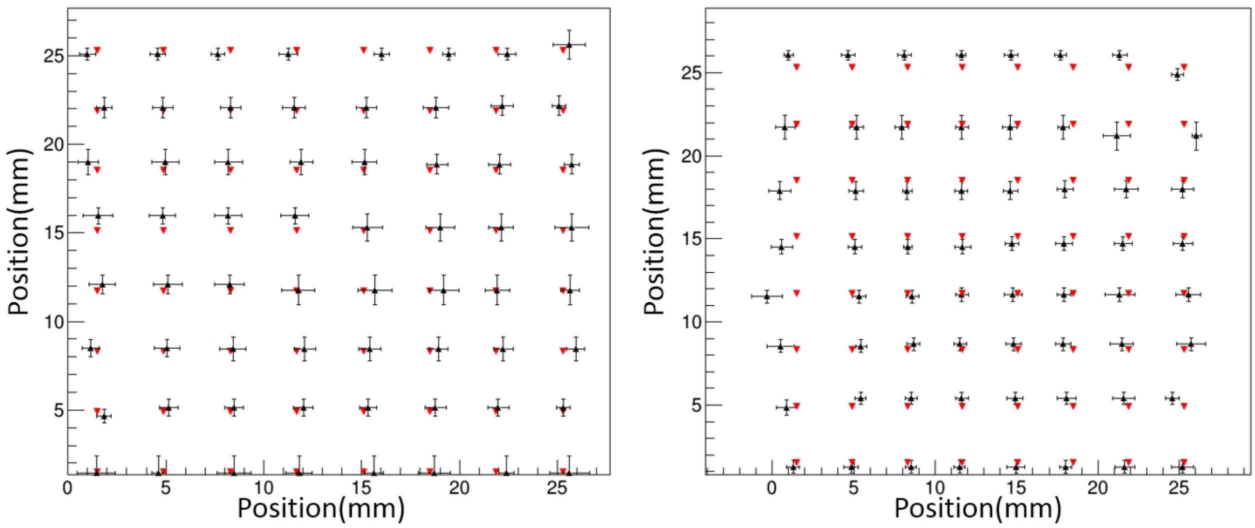


Fig. 9. The reconstruction result of the S-type detector(left) and B-type detector(right) using the photon distribution reconstruction method (PCB ($\phi$1.0, D3.4))

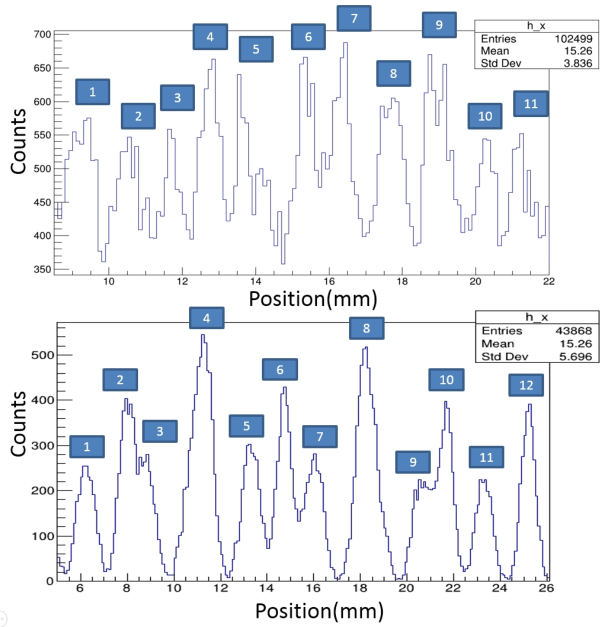


Fig. 10. The limit of position resolution of S-type detector-PCB(1.2,up).The limit of position resolution fo B-type detector-PCB(1.6,down)

of a 1 mm thick silicon detector and a 2 mm thick CdTe detector based on the pixel array semiconductor detector Timepix3, with a spatial resolution of up to 2.5 mm at 25 mm, which is one of the Compton Cameras with the most ideal imaging effect of the double-layer semiconductor detector structure today. The spatial resolution of the Compton Camera based on the whole scintillator is lower than that of the detector, mainly because the energy resolution of the scintillator detector is much lower than that of the semiconductor detector. However, the high processing cost of semiconductor detectors, harsh working conditions and complex electronic systems make it difficult to commercialize semiconductor-based Compton Cameras at low cost. The Compton Camera based on the monolithic scintillator crystal built in this study is low-cost, simple in structure, and slightly lower in detection performance than the semiconductor-based Compton Camera, which undoubtedly has greater possibilities in low-cost commercialization.

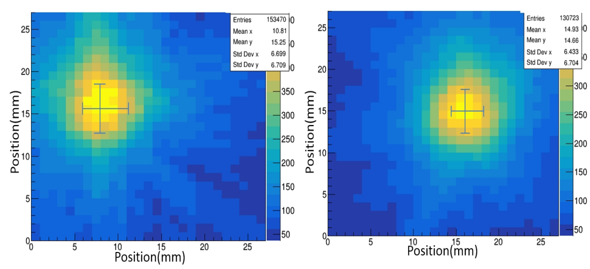


Fig. 11. The reconstruction results of Cs-137 at two points(8mm apart).

## VI. DISCUSSION

Most of the existing Compton Cameras use pixelated crystals to determine the position of the interaction position.[29, 30] There is no doubt that the higher pixelation, the higher accurate we can get. But as the level of pixelation increases, a series of problems arise. The following discussion only considers the case where the detector is scintillator detector, and

does not consider the case where the detector is semiconductor detector or gas detector. 1.The processing difficulty and cost of crystals will inevitably increase, and the level of pixelation cannot be increased indefinitely. Taking the 27*27*3 mm GAGG crystal used in this study as an example, if the pixelated crystal method is used to achieve 1.2 mm position resolution, the crystal pixels need to be divided into a 1.2*1.2*3 mm 23*23 array, and the processing cost will become 3-4 times. 2.In order to determine the interaction position, each pixel needs to have an independent data acquisition, with the increase of the level of pixelation, the acquisition system will become very redundant, and the redundant acquisition system will bring problems such as reduced signal-to-noise ratio and serious crosstalk. For example, in this study, the S-type detector achieves a position resolution of 1.2 mm using 32 data acquisition channels. If a traditional configuration is used to achieve the same position resolution, even using weighting calculation such as Anger logic, the number of data acquisition channels required would be significantly more than 32[31]. 3.Because the pixelated crystal must be coupled with the acquisition system one by one, its configuration can only be similar to the B-type detector in this study, and if the multi-layer B-type detector is used, there must be $\gamma$-ray to react with the electronic device instead of the crystal, which reduces the detector efficiency. The use of multi-layer S-type detectors will greatly reduce the efficiency degradation caused by this phenomenon.

In this study, we proposed a method for reconstructing the interaction position in monolithic crystals, and achieved good reconstruction accuracy, which can be used in many fields. In the study of nuclear reactions and nuclear structure, track measurement is an important research method, usually using equipment such as solid track detectors, ionization chambers or time projection chambers[32, 33], which mainly respond to charged particles and have low detection efficiency for $\gamma$-rays. In the future, the technology in this study can be used to combine multiple S-type detectors into a telescope detector system, which will obtain a good $\gamma$-rays trace. In the field of medical imaging, both single-photon emission computed tomography (SPECT) and positron emission tomography (PET) require accurate measurements of the interaction position of $\gamma$-rays. The detectors currently used are semiconductor detectors (CdTe, CZT, etc.) or pixelated scintillator detectors (CLYC, CsI,etc.)[34, 35]. The technology in this study can reduce costs, simplify the system structure, and improve the detection accuracy. In addition, this technology has the opportunity to play a role in the fields of $\mu$ imaging, radioactive survey, radiation protection, etc.

This study is only a preliminary study of the raction position reconstruction and the construction of Compton Cameras using monolithic crystals, and there is still a lot of work to be done. First of all, the S-type detector used a thin slice structure in this study, and the thickness of 3 mm can only be coupled with a layer of SiPM, which makes the z-direction cannot be determined, and only a fixed value can be taken. In the future, the thickness of the crystal can be increased, multilayer SiPM can be coupled, and the photon distribution can be used to determine the position in the z-direction. Secondly, the algorithm used in this study only considers the solid angle, but does not consider the optical transmission properties of photons in the crystal, which leads to the deterioration of the reconstruction accuracy of the edge part, and the optical transmission properties can be added to the algorithm to improve the reconstruction accuracy in the future. For the Compton Camera, the S-type detector is used as the scattering detector and the B-type detector is the two-layer configuration of the absorption detector, and the configuration of the multi-layer S-type detector can be used to improve the detection efficiency in the future.

## VII. CONCLUSION

In this paper, a prototype Compton Camera based on a monolithic GAGG crystal is built, with the S-type detector as the scattering detector and the B-type as the absorption detector. With two types of position reconstruction algorithm developed in the present work, the interaction position in the scattering and the absorption detectors can be determined with the resolution of 1.2 mm and 1.6 mm, respectively. Using Cs-137 as a point source, the position of the source can be determined with a resolution of 5.4 mm when the source was 27 mm away from the scattering detector.

The monolithic crystal based Compton Camera developed in the present work has the advantages of low cost, simple and compact in structure. The moderate imaging performance also meets the requirements of the radioactive source positioning and nuclear medicine in nuclear industry applications. These facts show the high potential of the monolithic crystal based Compton Camera to be commercialized.


[1] R.W.Todd, J.M.Nightingale, D.B.Everett, A proposed camera. Nature (251), 132-134(1974). doi: 10.1038/251132A0.

[2] Z. Yao, Y. Yuan, J. Wu et al., Rapid Compton camera imaging for source terms investigation in the nuclear decommissioning with a subset-driven origin ensemble algorithm. Radiat. Phys. Chem. 197, 110133 (2022).doi:10. 1016/j. radphyschem. 2022.110133

[3] J. Zhang, X. Liang, J. Cai et al., Prototype of an array SiPM-based scintillator Compton camera for radioactive materials detection. Radiat. Detect. Technol. 3(3), 17 (2019). doi:10.1007/s41605- 019- 0095-1

[4] F. Tian, C. Geng, Z. Yao et al., Radiopharmaceutical imaging based on 3D-CZT Compton camera with 3D-printed mouse phantom. Phys. Medica 96, 140–148 (2022). doi:org/ 10. 1016/j.ejmp. 2022. 03. 005

[5] R. Wu, C. Geng, F. Tian et al., GPU-accelerated three-dimensional reconstruction method of the Compton camera and its application in radionuclide imaging. Nucl. Sci. Tech. 34(4), 52 (2023). doi:org/ 10. 1007/ s41365- 023- 01199-y

[6] Z. Yao, Y. Xiao, B. Wang et al., Study of 3D fast compton

camera image reconstruction method by algebraic spatial sampling. Nucl. Instrum. Meth. A 954, 161345 (2018). doi: org/ 10. 1016/j.nima. 2018. 10. 023

[7] Z. Yao, C. Shi, F. Tian et al., Technical note: rapid and highresolution deep learning-based radiopharmaceutical imaging with 3D-CZT Compton camera and sparse projection data. Med. Phys.49(11), 7336–7346 (2022). doi:org/ 10. 1002/ mp. 15898

[8] Inc H. D. H100 Gamma-Ray Imaging Spectrometer[[EB/OL]. https://h3dgamma.com/H100Specs.pdf, 2022.2.3

[9] PHDS C. GeGI Gamma-Ray Imaging Spectrometer[EB/OL]. https://phdsco.com/wp-content/uploads/2022/02/20220216-GeGI-Front-and-Back.pdf,2022.2.3.

[10] Shinichiro T., Atsushi H., Yuto I.,et al. A Portable Si/CdTe Compton Camera and its Applications to the Visualization of Radioactive Substances. Nuclear Instruments and Methods in Physics Research Section A: Accelerators, Spectrometers, Detectors and Associated Equipment,doi:10.1016/J.NIMA.2014.11.119

[11] Xiaofeng G., Qingpei X., Dongfeng T.,et al. Simulation Study of the Backward-Scattering Effect in Compton Imager. Applied Radiation and Isotopes, 2017,124:93-99.doi:10.1016/j.apradiso.2017.03.019

[12] Liu Y., Fu J., Li Y.,et al. Preliminary Results of a Compton Camera Based On a Single 3D Position-Sensitive CZT Detector. Nuclear Science and Techniques,2018,29(10):145.doi:org/10.1007/s41365-018-0483-0

[13] Zhang Jipeng, Ma Xinhua, Zhang Bin et al.Simulation design and performance evaluation of the wide-energy range gamma-ray imaging detectors.Scientia Sinica(Technologica), 2024, 54: 31–42.doi: 10.1360/SST-2022-0411

[14] H. Muraishi, R.Enomoto, H.Katagiri*et al*.Visualization of low-level gamma radiation sources using a low-cost, high-sensitivity, omnidirectional compton camera. J. Vis. Exp.**2020**,155, e60463.doi: 10.3791/60463 .

[15] Z. Yao, Y. Xiao, M. Dong et al., Development of a two-layer dense-pixel LYSO Compton camera prototype for prompt gamma imaging. Phys. Med. Biol. 68, 045008 (2023). doi: org/ 10.1088/1361-6560/acb4d8

[16] T.Watanabe, R.Enomoto, H.Muraishi*et al*.Development of an omnidirectional gamma-ray imaging compton camera for low-radiation-level environmental monitoring. J. Appl. Phys.**2018**,57,026401.doi: 10.7567/JJAP.57.026401.

[17] H. Katagiri, W. Satoh, R. Enomoto *et al*.Development of an all-sky gamma-ray Compton camera based on scintillators for high-dose environments. J. Nucl. Sci.Technol.**2018**,55, 1172–1179.doi: 10.1080/00223131.2018.1485598.

[18] H. Muraishi, R.Enomoto, H.Katagiri*et al*.Visualization of low-level gamma radiation sources using a low-cost, high-sensitivity, omnidirectional compton camera. J. Vis. Exp.**2020**,155, e60463.doi: 10.3791/60463.

[19] R.K.Parajuli, M.Sakai, R. Parajuli*et al*. Development and Applications of Compton Camera—A Review.Sensors **2022**,22,7374. doi: 10.3390/s22197374.

[20] P.Buzhan.Silicon photomultiplier and its possible applications Nucl. Instrum. Methods Phys. Res. **504** 48–52. doi:10.1016/S0168-9002(03)00749-6.

[21] Min Li,Zhi-Min Wang,Cai-Mei Liu et al., Performance of compact plastic scintillator strips with wavelength shifting fibers using a photomultiplier tube or silicon photomultiplier readout. Nucl. Sci. Tech.**2020** 34:31.doi:10.1007/s41365-023-01175-6.

[22] Yu-Ying Li,Chang-Yu Li Kun Hu et al. Design and development of multi-channel front end electronics based on dual-polarity charge-to-digital converter for SiPM detector applications. Nucl. Sci. Tech.(2023) 34:18.doi:10.1007/s41365-023-01168-5

[23] Wei Lu,Lei Wang, Yong Yuan et al. Monte Carlo simulation for performance evaluation of detector model with a monolithic LaBr3(Ce) crystal and SiPM array for $\gamma$ radiation imaging. Nucl. Sci. Tech.(2022) 33:107.doi:10.1007/s41365-022-01081-3

[24] C.Z. Uche, W.H. Round, M.J. Cree, Evaluation of two compton Camera models for scintimammography. Nucl. Instrum. Meth. A.662(1), 55–60 (2012). doi:org/ 10.1016/j. nima.2011.09.058

[25] T.Yanagida , K.Kamada , Y.Fujimoto *et al*.Comparative study of ceramic and single crystal Ce:GAGG scintillator. Optical Materials **35**2480–2485(2013) doi:10.1016/j.optmat.2013.07.002.

[26] Wei-Jie Zhang, Qin-Hua Wei , Xiao Shen *et al*.Preparation and properties of GAGG:Ce/glass composite scintillation material. Chin. Phys. B. Vol. 30, No. 7 (2021) 074205. doi:10.1088/1674-1056/abe3ea

[27] Ji-Peng Zhang,Xiu-zuo Liang,Jia-le Cai*et al*.Prototype of an array SiPM-based scintillator Compton camera for radioactive materials detection. Radiation Detection Technology and Methods (2019) 3:17. doi:10.1007/s41605-019-0095-1

[28] D.Turecek, J.Jakubek, E.Trojanovaa *et al*.Compton camera based on Timepix3 technology. Journal of Instrumentation **13** C11022.doi:10.1016/j.optmat.2013.07.002.

[29] S.Takeda, S.Ishikawa, S.Odaka et al. A new Si/CdTe semiconductor Compton camera developed for high-angular resolution. In Hard X-Ray and Gamma-Ray Detector Physics IX; SPIE: Bellingham,WA, USA, 2007; **6706** pp:187-197.doi:10.1117/12.733840.

[30] E. Muñoz, J. Barrio, A. Etxebeste et al. A Performance evaluation of MACACO:a multilayer Compton camera. Physics in Medicine & Biology **62** (2017) 7321–7341 . doi:10.1088/1361-6560/aa8070.

[31] Ming-Hao Dong, Zhi-Yang Yao, Yong-Shun Xiao, Development and preliminary results of a large-pixel two-layer LaBr3 Compton camera prototype. Nuclear Science and Techniques **34** (2023) 34:121.doi:10.1007/s41365-023-01273-5.

[32] Duan Xiaojiao, LanXiaofei , TanZhixin et al. Calibration of CR-39 with monoenergetic protons. Nuclear Instruments and Methods in Physics Research A 609(2009)190–193. doi:10.1016/j.nima.2009.08.061.

[33] Chuan Huang, Zhiguo Xu, Zulong Zhao et al. Carbon ion radiography with a composite ionization chamber detector. Applied Radiation and Isotopes 203 (2024) 111072.doi:10.1016/j.apradiso.2023.111072.

[34] Hai-Yan Du, Cheng-Bo Du, Karl Giboni et al. Screener3D: a gaseous time projection chamber for ultra-low radioactive material screening. NUCL SCI TECH (2021) 32:142. doi:org/10.1007/s41365-021-00983-y

[35] A. Kishimoto, J. Kataoka, T. Nishiyama, et al. Performance and field tests of a handheld Compton camera using 3-D position-sensitive scintillators coupled to multi-pixel photon counter arrays.J. Instrum. **2014** ,9,P11025 doi:0.1088/1748-0221/9/11/P11025.